J. Fluid Mech. (2008), *vol.* 599, *pp.* 383–404.
doi:10.1017/S002211200800013X Printed in the United Kingdom

Analysis of sheet-like thermal plumes in turbulent Rayleigh–Bénard convection

OLGA SHISHKINA AND CLAUS WAGNER

DLR – Institute for Aerodynamics and Flow Technology, Bunsenstraße 10, 37073 Göttingen, Germany

(Received 14 June 2007 and in revised form 3 December 2007)

Sheet-like thermal plumes are investigated using time-dependent and three-dimensional flow fields obtained from direct numerical simulations and well-resolved large-eddy simulations of turbulent Rayleigh–Bénard convection in water (Prandtl number $Pr = 5.4$) in a cylindrical container with the aspect ratio $\Gamma = 1$ and for the Rayleigh numbers $Ra = 2 \times 10^9$ and 2×10^{10}.

To analyse quantitatively the physical properties of the sheet-like thermal plumes and the turbulent background and to obtain the temperature threshold which separates these two different flow regions, the temperature dependences of the conditionally averaged local heat flux, thermal dissipation rate and selected components of the velocity and vorticity fields are studied. It is shown that the sheet-like plumes are characterized by high values of the local heat flux and relatively large absolute values of the vertical components of the vorticity and velocity fields. The borders of these plumes are indicated by large values of the thermal dissipation rate and large absolute values of the horizontal vorticity components. In contrast to the sheet-like thermal plumes, the turbulent background is characterized by low values of the thermal dissipation rate, local heat flux and vertical vorticity component. The highest values of the local heat flux and the highest absolute values of the vertical vorticity component are found in the regions where the sheet-like plumes strike against each other. Fluid swirling at these places forms the stems of the mushroom-like thermal plumes which develop in the bulk of the Rayleigh–Bénard cell.

Further, formulae to calculate the curvature, thickness and length of the plumes are introduced. Geometrical properties such as plume area, diameter, curvature, thickness and aspect ratio together with the physical properties of the sheet-like plumes such as temperature, heat flux, thermal dissipation rate, velocity and vorticity are investigated.

1. Introduction

The subject of most of the fundumental thermal convection studies is the classical Rayleigh–Bénard convection (RBC) (see, for example, Siggia 1994; Grossmann & Lohse 2000; Kadanoff 2001; Verzicco & Camussi 2003; Ahlers 2005; Hartlep, Tilgner & Busse 2005; Shishkina & Wagner 2007*b*; du Puits *et al.* 2007). Inside a Rayleigh–Bénard cell, turbulent motion of the fluid develops if the temperature difference between a heated bottom plate and a cooled top plate of the container is large enough. Flow visualizations in experimental studies of turbulent RBC using various fluids revealed large coherent structures which have a mushroom-like form, when viewed from the side (Sparrow, Husar & Goldstein 1970; Zocchi, Moses & Libchaber 1990; Xi, Lam & Xia 2004) and a sheet-like form when viewed from above (Funfschilling & Ahlers 2004; Haramina & Tilgner 2004; Puthenveettil & Arakeri

2005). These structures are called thermal plumes. The thermal plumes play an important role in stellar convection. They are observed at the top of the convection zones (see, for example, Zahn 2000) as flow structures desending towards the hot centres of the stars.

Because of the temperature difference between these large flow structures and the surrounding fluid and, hence, owing to different refractive indices in these parts of the fluid, the thermal plumes become visible. Although the thermal plumes can be seen easily in experiments, the problem of their extraction is not satisfactorily solved. Thresholds of certain quantities such as the temperature (Zhou & Xia 2002) and/or the vertical velocity (Juliem *et al.* 1999; Ching *et al.* 2004), the skewness of the temperature derivative (Belmonte & Libchaber 1996) or the local thermal dissipation rate (Shishkina & Wagner 2006) have been used for plume identification so far. A proper choice of the threshold value which separates explicitly the large coherent structures from the background fluid still remains one of the unresolved problems.

The thermal plume lifecycle has been one of the main subjects of recent studies of turbulent RBC (Puthenveettil & Arakeri 2005). Generally, the plumes are generated in the thermal boundary layers close to the bottom or the top plate and are driven to the opposite plate by buoyancy. In the bulk the thermal plumes have a mushroom-like form, while at the borders between the boundary layers and the bulk or slightly deeper in the bulk are situated the sheet-like roots (or 'mycelium theads') of the plumes (Shishkina & Wagner 2006). Xi *et al.* (2004) showed by experiment that for high Rayleigh numbers and relatively small aspect ratios of the Rayleigh–Bénard cells, the thermal plumes initiate the large-scale motion evolution.

Zhou, Sun & Xia (2007) studied turbulent RBC in water and showed that the area of the sheet-like plumes exhibits log-normal distribution. The plume extraction was conducted manually and was based on temperature thresholds. This study also revealed that the sheet-like thermal plumes move across the plate, interact and merge to generate the mushroom-like plumes. The regions of these sheet-like plume interactions are characterized by large values of the vertical vorticity. This was also assumed in the work by Cortese & Balachandar (1993), who performed numerical simulations of RBC for the Rayleigh number of order 10^7.

In the present paper, we propose an approach for the numerical investigation of the sheet-like thermal plumes. We consider the same values of the Rayleigh number ($Ra = 2 \times 10^9$ and 2×10^{10}), Prandtl number ($Pr = 5.4$) and the aspect ratio ($\Gamma = 1$) as realized by Zhou *et al.* (2007) in their experiments. To extract the sheet-like plumes we use temperature thresholds which are defined based on the analysis of the thermal dissipation rates.

The paper is organized as follows. In § 2, the governing equations and their dimensionalization are presented together with some details on the numerical method. The problem of the sheet-like plume extraction is discussed in § 3. In § 4, geometrical properties such as area, curvature, thickness, length and aspect ratio of the sheet-like plumes are defined and investigated. Physical characteristics of the plumes, i.e. temperature, velocity, vorticity, heat flux and thermal dissipation rate, are discussed in § 5.

2. Governing equations and simulations parameters

The governing momentum, energy and continuity equations for the Rayleigh–Bénard problem in Boussinesq approximation can be written, respectively, as follows

$$\hat{\boldsymbol{u}}_t + \hat{\boldsymbol{u}} \cdot \nabla \hat{\boldsymbol{u}} + \rho_0^{-1} \nabla \hat{p} = \nu \Delta \hat{\boldsymbol{u}} + \alpha g (\hat{T} - \hat{T}_0) \boldsymbol{e}_z, \tag{2.1a}$$

$$\hat{T}_t + \hat{\boldsymbol{u}} \cdot \nabla \hat{T} = \kappa \Delta \hat{T}, \tag{2.1b}$$

$$\nabla \cdot \hat{\boldsymbol{u}} = 0, \tag{2.1c}$$

where $\hat{\boldsymbol{u}}$ is the velocity vector-function, $\hat{T}$ the temperature, $\hat{\boldsymbol{u}}_t$ and $\hat{T}_t$ their time derivatives, $\hat{p}$ the pressure, ρ_0 the density and $\boldsymbol{e}_z$ the unit vector in the vertical direction. On substituting the factorization $\hat{v} = v_{ref}\, v$ for each dimensioned variable $\hat{v}$ in (2.1), where v is a dimensionless variable and v_{ref} the reference value, $\hat{x}_{ref} = \hat{D}$, $\hat{u}_{ref} = (\alpha g \hat{D}\, \delta\hat{T})^{1/2}$, $\hat{t}_{ref} = \hat{x}_{ref}/\hat{u}_{ref}$, $\hat{T}_{ref} = \delta\hat{T}$, $\hat{p}_{ref} = \hat{u}_{ref}^2\, \rho_0$, we obtain the following system of dimensionless three-dimensional equations in a cylindrical domain Υ with the diameter $D = 1$ and the height $H = \Gamma^{-1}$:

$$\boldsymbol{u}_t + \boldsymbol{u}\cdot\nabla\boldsymbol{u} + \nabla p = \mu\Delta\boldsymbol{u} + T\boldsymbol{e}_z, \tag{2.2a}$$

$$T_t + \boldsymbol{u}\cdot\nabla T = \mu Pr^{-1}\Delta T, \tag{2.2b}$$

$$\nabla\cdot\boldsymbol{u} = 0, \tag{2.2c}$$

with $\mu = \Gamma^{-3/2} Ra^{-1/2} Pr^{1/2}$. The dimensionless temperature varies between $T|_{z=0} = +0.5$ at the bottom and $T|_{z=H} = -0.5$ at the top horizontal walls and satisfies $\partial T/\partial\boldsymbol{n} = 0$ on the vertical walls, where $\boldsymbol{n}$ is the normal vector. According to the impermeability and no-slip conditions, the velocity field vanishes on the boundary, i.e. $\boldsymbol{u}|_{\partial\Upsilon} = 0$.

To investigate sheet-like thermal plumes, we simulated turbulent Rayleigh–Bénard convection in a fluid with Prandtl number $Pr = 5.4$ which corresponds to water. The aspect ratio of the cylindrical container equals $\Gamma = 1$ and the considered Rayleigh numbers are 2×10^9 and 2×10^{10}. The simulations were performed with the fourth-order-accurate finite-volume method developed for solving (2.2) in cylindrical coordinates (z, φ, r) on staggered structured non-equidistant grids (Shishkina & Wagner 2007*a*).

The computational mesh used in the simulations consists of $220\times512\times96$ nodes in the vertical, azimuthal and radial directions, respectively. The mesh nodes are distributed equidistantly in the azimuthal direction and are clustered in the vicinity of the rigid walls to resolve the viscous and thermal boundary layers. For the case $Ra = 2\times10^9$, the mesh satisfies the spatial resolution requirements by Grötzbach (1983) both in the bulk and in the vicinity of the rigid walls and, hence, it is fine enough to resolve all relevant turbulent scales in the direct numerical simulation (DNS). This is the case for the following reasons.

According to Grötzbach (1983), the computational mesh used in the DNS must satisfy the following requirement

$$h_{V_i} \leqslant \pi\eta_{V_i}(Ra)\min\{1; Pr^{-3/4}\} \tag{2.3}$$

on each finite volume V_i, where $h_{V_i} = (\Delta z_i\, r_i \Delta\varphi_i\, \Delta r_i)^{1/3}$ is the mesh width and

$$\eta_{V_i}(Ra) = \mu^{3/4}\epsilon_u^{-1/4}$$

denotes the Kolmogorov scale on this finite volume. Here ϵ_u is the turbulent kinetic energy dissipation rate, which in Cartesian coordinates reads

$$\epsilon_u = \frac{\mu}{2}\sum\left(\frac{\partial u_i'}{\partial x_j} + \frac{\partial u_j'}{\partial x_i}\right)^2$$

with u_i' the fluctuation of the velocity component u_i with respect to the mean velocity field. In the case $Pr = 5.4$, the requirement (2.3) can be rewritten as

$$\frac{h_{V_i}}{\eta_{V_i}(Ra)} \leqslant \pi Pr^{-3/4} \approx 0.887. \tag{2.4}$$

Close to the rigid walls the $\eta_{V_i}(Ra)$-values and, hence, the required mesh width are small, while in the bulk they are relatively large. In figure 1, the computational mesh

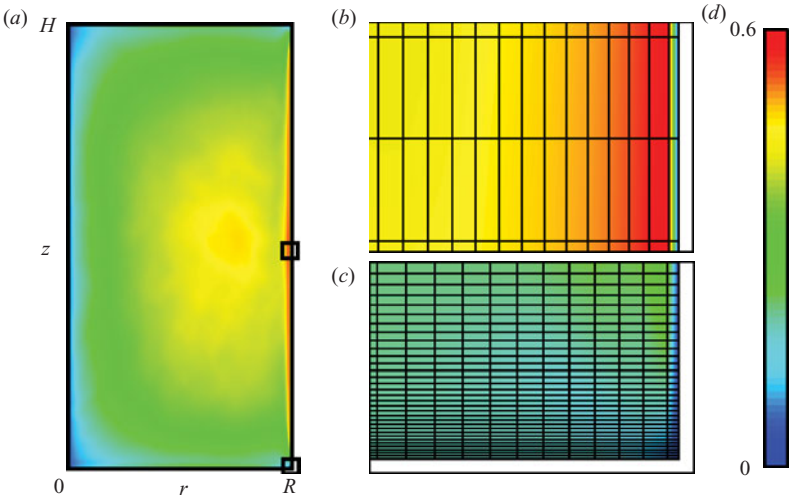

FIGURE 1. (*a*) Spatial distribution of the ratio between the mesh width h_{V_i} and the Kolmogorov scale η_{V_i} for the case $Ra = 2 \times 10^9$, $Pr = 5.4$ and $\Gamma = 1$, $h_{V_i}/\eta_{V_i} \leqslant 0.64$; (*b*, *c*) close-up views (50-times zoom) together with superimposed computational mesh; (*d*) colour scale for h_{V_i}/η_{V_i}.

in the radial r- and axial z-directions is presented together with the distribution of the ratio between the mesh width and the Kolmogorov scale, i.e. the function h_{V_i}/η_{V_i} in these directions as it was evaluated from the numerical data for $Ra = 2 \times 10^9$. We can see that the highest values of h_{V_i}/η_{V_i} are located in the vicinity of the vertical wall. Although in the case $Ra = 2 \times 10^9$ the requirement (2.4) of the mesh applicability in the DNS is fulfilled, since

$$\max_{V_i} h_{V_i}/\eta_{V_i}(2 \times 10^9) \leqslant 0.64,$$

the inequality (2.4) fails for $Ra = 2 \times 10^{10}$, since $\max_{V_i} h_{V_i}/\eta_{V_i}(2 \times 10^{10}) = 1.36$ in this case. Therefore to simulate turbulent RBC for $Ra = 2 \times 10^{10}$ we conducted a large-eddy simulation (LES) using the tensor-diffusivity subgrid scale model by Leonard & Winckelmans (1999). According to this model, the subgrid scale stress tensors are approximated by the first term of the exact series expansions for filtered products. For further details on the numerical method and the subgrid modelling used in the simulations, we refer to Shishkina & Wagner (2007*c*).

In figures 2 and 3, the instantaneous temperature distribution $-0.5 \leqslant T \leqslant 0.5$ is visualized for the case $Ra = 2 \times 10^9$, $Pr = 5.4$, $\Gamma = 1$ in a central vertical plane (figure 2*a*) and in horizontal cross-sections (figure 3) at distances $z = H/Nu$, $z = H/2$ and $z = H(1 - 1/Nu)$ from the top plate. These figures give an impression of the complicated three-dimensional flow structures which develop in turbulent RBC. In figures 3(*a*) and 3(*c*) (as well as in figure 9) small wave-like structures are observed, which develop near the sheet-like thermal plumes and replicate their form. These structures do not correlate with the mesh used in the simulations and the associated wavelength is up to 10 times larger than the mesh width in these regions. Therefore we conclude that they reflect some physical effects for which we have no explanation so far.

Further, in figure 2(*b*, *c*) snapshots of the vertical component of the velocity and the local heat flux distributions are presented. The snapshot of the vertical velocity (figure 2*b*) reflects a large-scale circulation which developes in turbulent RBC for high

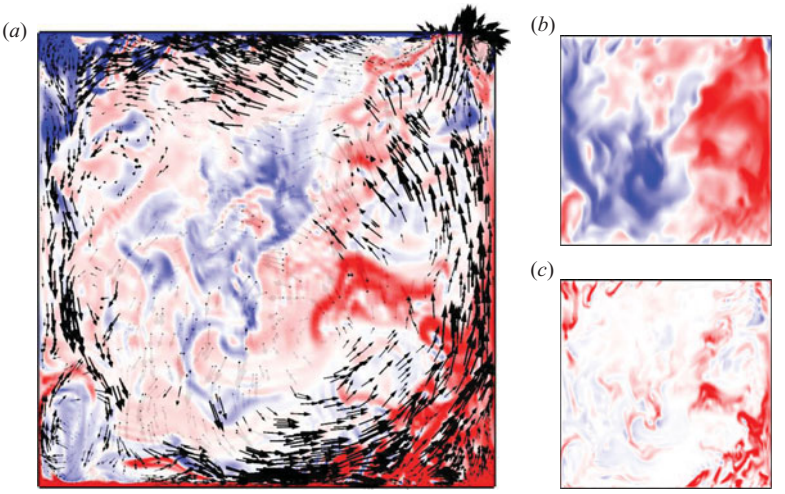

FIGURE 2. Snapshots of (*a*) the temperature field $-0.5 \leqslant T \leqslant 0.5$ with superimposed velocity vectors, (*b*) the vertical velocity $-0.3 \leqslant u_z \leqslant 0.3$ and (*c*) the local heat flux for $Ra = 2 \times 10^9$, $Pr = 5.4$, $\Gamma = 1$ in a central vertical cross-section. The colour scale ranges from blue (negative values) through white (zero) to red (positive values).

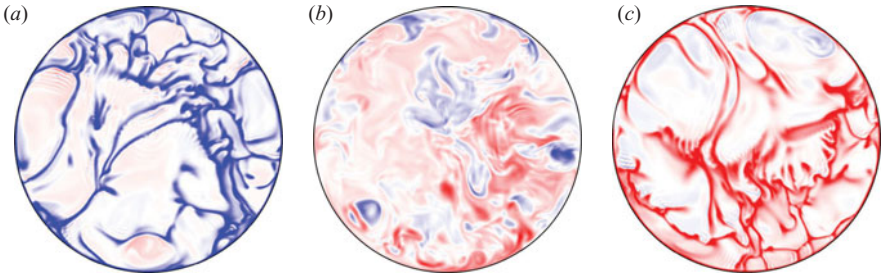

FIGURE 3. Snapshots of the temperature field for $Ra = 2 \times 10^9$, $Pr = 5.4$, $\Gamma = 1$ in horizontal cross-sections at distances (*a*) $z = H/Nu$, (*b*) $z = H/2$ and (*c*) $z = H - H/Nu$ from the top plate. The colour scale is as figure 2.

Rayleigh numbers and $\Gamma = 1$. Comparing figure 2(*a*) with figure 2(*c*), we conclude that in the vertical cross-sections, large values of the local heat flux correspond generally to the thermal plumes.

Evaluating the Nusselt number

$$Nu = \Gamma^{1/2} Ra^{1/2} Pr^{1/2} \langle u_z T \rangle_{t,S_z} - \Gamma^{-1} \left\langle \frac{\partial T}{\partial z} \right\rangle_{t,S_z},$$

where $\langle \cdot \rangle_{t,S_z}$ denotes time- and area-averaging over any (φ, r)-plane S_z at distance z from the top plate, we obtained $Nu = 81 \pm 1.2\%$ ($Ra = 2 \times 10^9$) and $Nu = 210 \pm 2.3\%$ ($Ra = 2 \times 10^{10}$). The statistical averaging of the data was conducted for 101 and 75 dimensionless time units in the former and in the latter cases, respectively. The obtained values agree well with those obtained from the scaling law $Nu = (0.19 \pm 0.01) Ra^{0.28 \pm 0.06}$ derived by Lui & Xia (1998) and Shang *et al.* (2004) from their experimental data. The Nusselt numbers obtained in the simulations for $Ra = 2 \times 10^9$ are also in good agreement with measurements by Funfschilling *et al.* (2005) for $Pr = 4.38$ and $\Gamma = 1$. For higher Rayleigh numbers, the LES predicts Nusselt numbers,

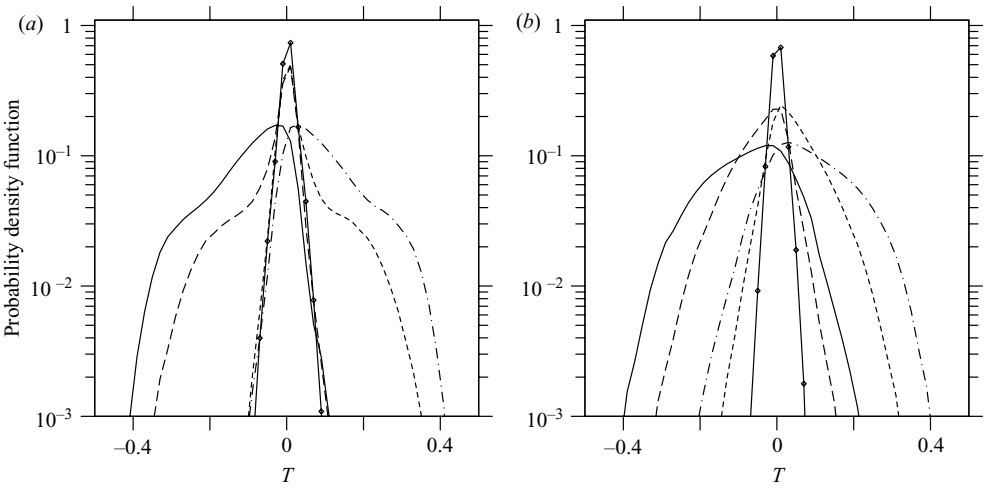

FIGURE 4. Probability density functions of the temperature, evaluated for (*a*) $Ra = 2 \times 10^9$ and (*b*) $Ra = 2 \times 10^{10}$, $Pr = 5.4$, $\Gamma = 1$ and distances $z = 0.5H/Nu$ (——), $z = H/Nu$ (– – –), $z = H/2$ (—•—), $z = H(1 - 1/Nu)$ (- - -) $z = H(1 - 0.5/Nu)$ (– · –) from the top plate.

which exceed those obtained in experiments using relatively small containers. For example, in measurements by Funfschilling *et al.* (2005), non-Oberbeck–Boussinesq effects are present, since the considered temperature differences between the bottom and the top plates are higher than those of the region of validity of the Boussinesq approximation for water (see Gray & Giorgini 1976). These non-Oberbeck-Boussinesq effects lead to lower Nusselt number (see Ahlers *et al.* 2006) in comparison to the Boussinesq case considered in numerical simulations if the operating fluid is water. Although the simulated mean heat flux is sensitive to the subgrid scale model used in LES, in the well-resolved LES this influence is insignificant.

3. Sheet-like plumes extraction

The absolute temperature inside the sheet-like thermal plumes is higher than that of the background fluid. Based on this temperature difference, the plumes can be distinguished from the surrounding fluid.

Zhou *et al.* (2007), who investigated turbulent RBC in water for $Ra = 2 \times 10^9$ and $Pr = 5.4$, used thermochromic liquid crystal microspheres to visualize the sheet-like plumes in horizontal cross-sections of the cylindrical Rayleigh–Bénard cell. They were able to estimate the temperature values analysing 31% of the temperature scale which corresponds to the temperature-sensitive colour range of the particles. In our numerical simulations, the complete temperature and velocity fields are obtained and are available in all points of the domain. The probability density functions (p.d.f.) of the temperature evaluated for $Ra = 2 \times 10^9$ and 2×10^{10}, $Pr = 5.4$, $\Gamma = 1$ and different distances from the top plate are shown in figure 4. The p.d.f.s encompass all the data from each considered cross-section. We can see that the observed temperature range is contracting with increasing distance from the horizontal plates. Although the temperature p.d.f. over the whole Rayleigh–Bénard cell is a symmetric function with respect to $T = 0$, the temperature p.d.f. over a horizontal cross-section is generally non-symmetric. The graphs of the temperature p.d.f. for any horizontal cross-sections at distances z and $(H - z)$ from the top plate are reflection symmetric with respect to $T = 0$. The peak-like shape of the temperature p.d.f. in the centre horizontal

cross-section is associated with the uniformity of the background in the bulk, while the skewed distribution near the horizontal plates reflects the preponderance of the thermal plumes in these regions.

Further, to determine the temperature threshold which separates the sheet-like plumes from the background fluid we investigate the dependences on the temperature of conditionally averaged quantities, such as convective vertical heat flux

$$\theta = \Gamma^{1/2} Ra^{1/2} Pr^{1/2} u_z T - \Gamma^{-1} \frac{\partial T}{\partial z},$$

thermal dissipation rate

$$\epsilon_\theta = \Gamma^{-3/2} Ra^{-1/2} Pr^{-1/2} (\nabla T)^2,$$

velocity and vorticity in the vertical and horizontal directions. In a fixed horizontal cross-section S_z of the Rayleigh–Bénard cell and a certain temperature interval $[T_k, T_{k+1}[$ the conditionally averaged value $\overline{\varphi}(T_k \leqslant T < T_{k+1})$ of a certain quantity φ is obtained by averaging φ in time and over those parts of S_z, which correspond to the temperature interval $[T_k, T_{k+1}[$, as follows

$$\overline{\varphi}(T_k \leqslant T < T_{k+1}) = \frac{C \langle \varphi \ \vartheta(T_k \leqslant T < T_{k+1}) \rangle_{t,S_z}}{\langle \vartheta(T_k \leqslant T < T_{k+1}) \rangle_{t,S_z}},$$

where C denotes a certain normalizing constant and

$$\vartheta(T_k \leqslant T < T_{k+1}) = \mathscr{H}(T - T_k) - \mathscr{H}(T - T_{k+1}),$$

with $\mathscr{H}(x)$ the Heaviside function, i.e. $\mathscr{H}(x) = 1$ if $x \geqslant 0$ and $\mathscr{H}(x) = 0$ otherwise. Thus, in the temperature interval $[T_k, T_{k+1}[$ the conditionally averaged values of the vertical velocity $\overline{u_v}$, the absolute value of the horizontal velocity $\overline{|u_h|}$, the heat flux $\overline{\theta}$, the thermal dissipation rate $\overline{\epsilon_\theta}$ and the absolute values of the vertical $\overline{|\omega_v|}$ and horizontal $\overline{|\omega_h|}$ vorticities are calculated as follows

$$\begin{aligned}
\overline{u_v} &= C_u \langle u_v \ \vartheta \rangle_{t,S_z} \langle \vartheta \rangle_{t,S_z}^{-1}, \\
\overline{|u_h|} &= C_u \langle |u_h| \ \vartheta \rangle_{t,S_z} \langle \vartheta \rangle_{t,S_z}^{-1}, \\
\overline{\theta} &= C_\theta \langle \theta \ \vartheta \rangle_{t,S_z} \langle \vartheta \rangle_{t,S_z}^{-1}, \\
\overline{\epsilon_\theta} &= C_{\epsilon_\theta} \langle \epsilon_\theta \ \vartheta \rangle_{t,S_z} \langle \vartheta \rangle_{t,S_z}^{-1}, \\
\overline{|\omega_v|} &= C_\omega \langle |\omega_v| \ \vartheta \rangle_{t,S_z} \langle \vartheta \rangle_{t,S_z}^{-1}, \\
\overline{|\omega_h|} &= C_\omega \langle |\omega_h| \ \vartheta \rangle_{t,S_z} \langle \vartheta \rangle_{t,S_z}^{-1},
\end{aligned}$$

with normalizing constants C_u, C_θ, C_{ϵ_θ} and C_ω.

In figure 5, the conditionally averaged values of the vertical velocity component, the absolute value of the horizontal velocity component, the heat flux, the thermal dissipation rate and the absolute values of the vertical and horizontal vorticity components are presented. The values were obtained from the numerical data for $Ra = 2 \times 10^9$ and 2×10^{10}, $Pr = 5.4$, $\Gamma = 1$ and different distances from the top plate. Here the bin width is 0.02 and the normalizing constants C_u, C_θ, C_{ϵ_θ} and C_ω equal, respectively,

$$\begin{aligned}
C_u &= \min\{c_{u_v}, c_{|u_h|}\}, \\
C_\theta &= c_\theta, \\
C_{\epsilon_\theta} &= c_{\epsilon_\theta}, \\
C_\omega &= \min\{c_{|\omega_v|}, c_{|\omega_h|}\}
\end{aligned}$$

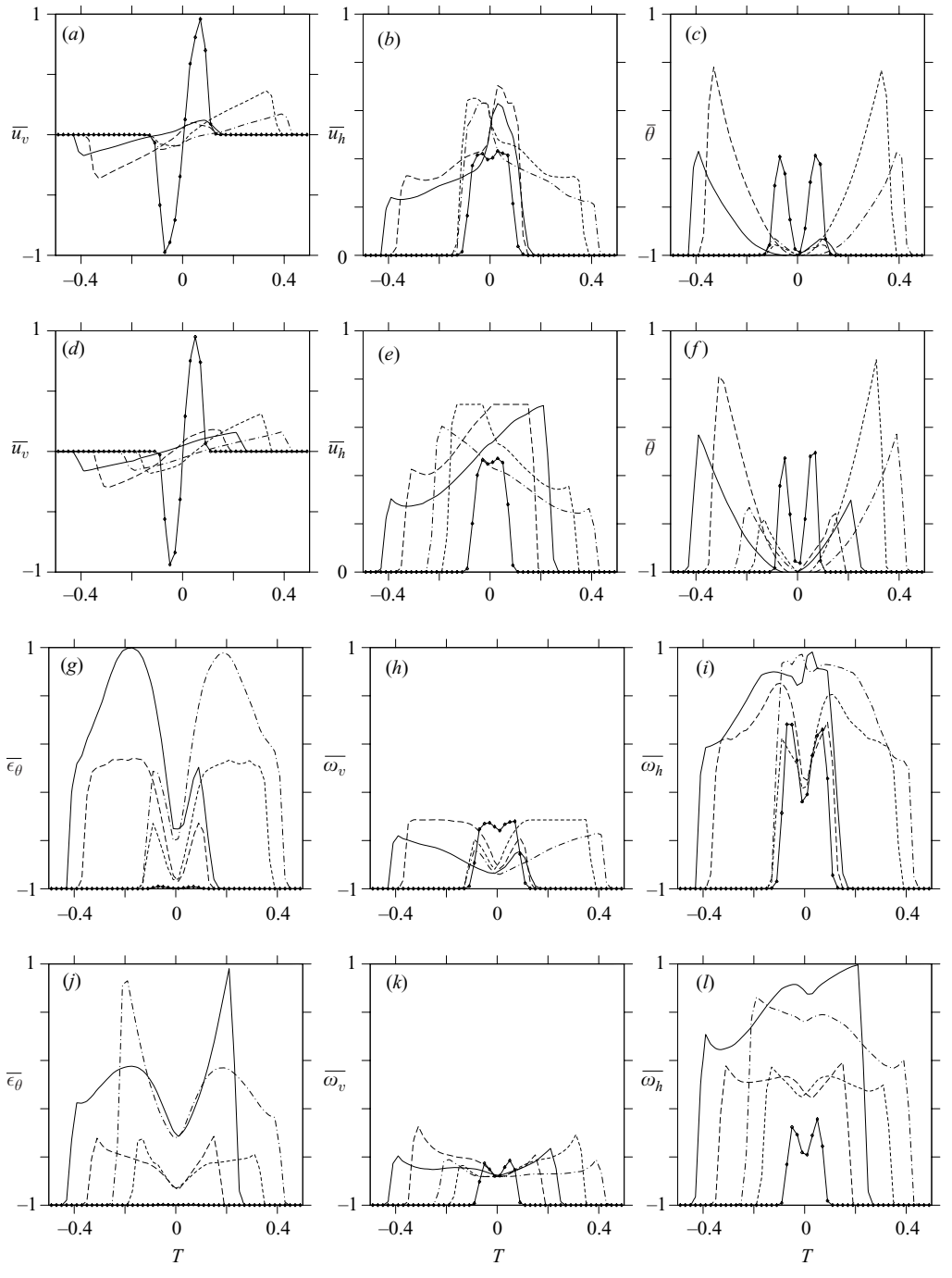

FIGURE 5. Conditionally averaged values of the vertical velocity component (a, d), the absolute value of the horizontal velocity component (b, e), heat flux (c, f), thermal dissipation rate (g, j), absolute values of the vertical (h, k) and horizontal (i, l) vorticity components, evaluated for $Ra = 2 \times 10^9$ (a–c, g–i) and $Ra = 2 \times 10^{10}$ (d–f, j–l), $Pr = 5.4$, $\Gamma = 1$ and distances $z = 0.5H/Nu$ (——), $z = H/Nu$ (– – –), $z = H/2$ (—•—), $z = H(1-1/Nu)$ (- - -) $z = H(1-0.5/Nu)$ (– · –) from the top plate.

with

$$c_\varphi = \left(\max_{z\in[0,H]} \max_{T\in[-0.5,0.5]} \left\{ \langle \varphi\, \vartheta \rangle_{t,S_z} \langle \vartheta \rangle_{t,S_z}^{-1} \right\} \right)^{-1}.$$

Figure 5 reflects the dependencies of the above presented quantities on the temperature. For example, the conditionally averaged vertical velocity component is positive (or negative) for positive (or negative) values of the temperature (figure 5*a*, *d*). Just like the probability density functions for the temperature (figure 4) the graphs of the conditionally averaged quantities (figure 5) for any distances z and $(H - z)$ from the top plate look reflection symmetric with respect to $T = 0$.

While relatively large absolute values of the temperature in figure 5 correspond to the interior of the sheet-like thermal plumes, the regions with the temperature values around zero are associated with the background fluid. Without fixing the temperature threshold which separates the sheet-like plumes from the surrounding fluid, we can give the following qualitative description of the physical properties of these two different parts of fluid, i.e. the sheet-like plumes and the turbulent background. The interior of the sheet-like thermal plumes and the background fluid are indicated, respectively, by large and small absolute values of the vertical velocity component (figure 5*a*, *d*), the local heat flux (figure 5*c*, *f*) and the vertical vorticity component (figure 5*h*, *k*). In contrast to the vertical velocity component, large absolute values of the horizontal velocity component are obtained outside the sheet-like plumes, while inside the plumes these values are relatively small (figure 5*b*, *e*). The turbulent background is also indicated by small values of the thermal dissipation rate (figure 5*g*, *j*).

Finally, we address the question of which temperature threshold separates the sheet-like thermal plumes from the turbulent background and indicates the borders of the sheet-like plumes. Considering the solid lines in figure 5 which correspond to the border between the upper cold thermal boundary layers and the bulk ($z = 0.5H/Nu$), we can see that within the temperature interval $-0.35 \leqslant T \leqslant 0$ which includes the desired temperature threshold, most of the considered characteristics such as the conditionally averaged vertical (figure 5*a*, *d*) and horizontal (figure 5*b*, *e*) velocity components, heat flux (figure 5*c*, *f*) or vertical vorticity component (figure 5*h*, *k*) have an almost monotonous dependency on the temperature. These quantities do not change qualitatively within the interval $-0.35 \leqslant T \leqslant 0$. Therefore they cannot provide the threshold we are looking for.

On the border between the upper cold thermal boundary layer and the bulk ($z = 0.5H/Nu$), the conditionally averaged thermal dissipation rate (figure 5*g*, *j*) has a well-pronounced extremum within the temperature interval $T \in [-0.35, 0]$, which corresponds to the temperature $T = T_{thr}^{-}(z)$. This means that the temperature $T = T_{thr}^{-}(z)$ corresponds generally to the maximum value of the conditionally averaged thermal dissipation rate, i.e. to the borders between the sheet-like plumes and the surrounding fluid in the horizontal cross-section S_z at a distance $z = 0.5H/Nu$ from the top plate. Therefore to extract the sheet-like plumes at the border between the upper cold thermal boundary layer and the bulk, we can use the temperature threshold $T = T_{thr}^{-}(z)$. Analogously, at the border between the lower warm boundary layer and the bulk ($z = H - 0.5H/Nu$), the desired temperature threshold $T = T_{thr}^{+}(z)$ corresponds to the maximum value of the conditionally averaged thermal dissipation rate within the interval $T \in [0, 0.35]$. For the case $Ra = 2 \times 10^9$, $Pr = 5.4$ and $\Gamma = 1$ we found $T_{thr}^{-}(0.5H/Nu) \approx -0.18$ and $T_{thr}^{+}(H - 0.5H/Nu) \approx 0.18$.

Another important observation is that within the interval $T \in [-0.35, 0]$, the conditionally averaged absolute value of the horizontal vorticity component has

its maximum close to $T = T^-_{thr}$ (figure 5*i*, *l*). This means that in the vicinity of the sheet-like thermal plumes, the absolute values of the horizontal vorticity component are high. Thus, large absolute values of the horizontal vorticity component indicate the borders of the sheet-like thermal plumes not only close to the horizontal plates, but also deeper in the bulk.

While moving away from the plates ($z = 0$ or $z = H$) towards the bulk (up to $z = H/Nu$ or $z = H(1 - 1/Nu)$, respectively) the conditionally averaged absolute values of all components of the velocity field (figure 5*a*, *b*, *d*, *e*), the local heat flux (figure 5*c*, *f*) and the vertical vorticity component (figure 5*h*, *k*) generally increase, while the conditionally averaged thermal dissipation rate (figure 5*g*, *j*) and absolute value of the horizontal vorticity component (figure 5*i*, *l*) decrease.

4. Geometrical properties of the sheet-like plumes

Warm and cold sheet-like thermal plumes are identified as geometrical objects in any horizontal cross-sections S_z at a distance z from the top plate as simply connected subdomains of S_z, restricted by the plume temperature thresholds T^+_{thr} and T^-_{thr}, respectively, as follows

$$\mathscr{P}^+ = \{(x, y) \in S_z : T(x, y) \in [T^+_{thr}, 0.5]\}, \quad z \geqslant H/2,$$

and

$$\mathscr{P}^- = \{(x, y) \in S_z : T(x, y) \in [-0.5, T^-_{thr}]\}, \quad z \leqslant H/2.$$

Here the vertical coordinate z and time t are omitted.

According to § 3, at the borders between the boundary layers and the bulk ($z = 0.5H/Nu$ and $z = H - 0.5H/Nu$, respectively) the temperature thresholds T^-_{thr} and T^+_{thr} are defined as points of maximum conditionally averaged thermal dissipation rate in S_z (see figure 5*g*, solid line). In the bulk, the point of the local maximum of the conditionally averaged horizontal vorticity component (figure 5*i*) or any other reasonable temperature threshold can serve as $T^\pm_{thr}$. For example, at distance $z = H/Nu$ from the top plate (figure 5) the graphic of the conditionally averaged thermal dissipation rate (figure 5*g*) is almost flat within the interval $T \in [-0.35, -0.14]$ and dramatically decreases for $T \in]-0.14, 0]$. At the same distance from the top plate the conditionally averaged horizontal vorticity component (figure 5*i*) has its maximum within the interval $T \in [-0.14, -0.12]$. Therefore we select the temperature thresholds $T^-_{thr}(H/Nu) = -0.14$ and $T^+_{thr}(H - H/Nu) = 0.14$ to extract sheet-like thermal plumes in the cross-sections S_z at distances $z = H/Nu$ and $z = H - H/Nu$ from the top plate.

In figure 6, the extracted cold sheet-like plumes which are obtained using the plume temperature threshold $T^-_{thr} = -0.14$ at distance $z = H/Nu$ from the top plate for the case $Ra = 2 \times 10^9$, $Pr = 5.4$, $\Gamma = 1$, are presented. In our plume analysis we consider the sheet-like thermal plumes, the relative area of which,

$$A_{\mathscr{P}} = |\mathscr{P}|/|S_z|,$$

is larger than 0.02%, where $|\mathscr{P}|$ and $|S_z|$ denote the areas of $\mathscr{P}$ and S_z, respectively. In figure 6, the sheet-like plumes, the relative area of which is less than 0.1%, are also omitted. The total number of the plumes extracted at fixed time in the cross-section S_z is denoted by $\mathscr{N}_{\mathscr{P}}$ and is 28 in the example considered in figure 6.

We define the plume diameter $D_{\mathscr{P}}$ as the maximum distance between any two points in $\mathscr{P}$,

$$D_{\mathscr{P}} = \max_{(x_1,y_1)\in\mathscr{P},\,(x_2,y_2)\in\mathscr{P}} ((x_1 - x_2)^2 + (y_1 - y_2)^2)^{1/2},$$

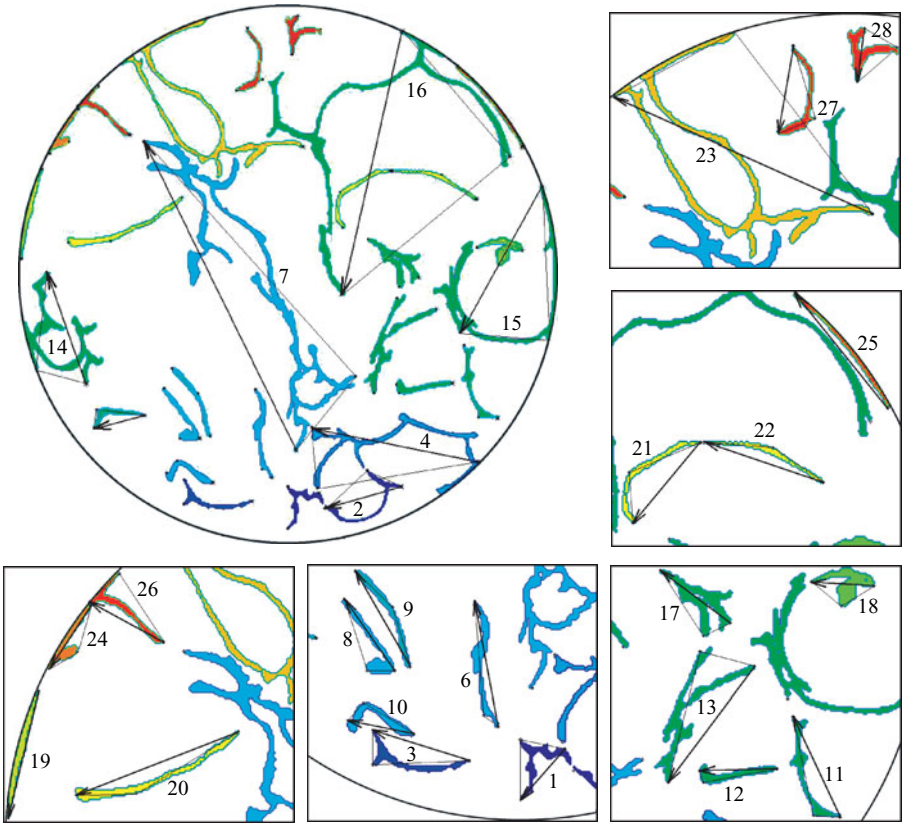

FIGURE 6. Thermal plumes extracted for the case $Ra = 2 \times 10^9$, $Pr = 5.4$, $\Gamma = 1$, $T^-_{thr} = -0.14$ at distance $z = H/Nu$ from the top plate. Colour scale is due to plume enumeration. For each plume $\mathscr{P}$ the arrow goes from (x_2^*, y_2^*) to (x_1^*, y_1^*) and corresponds to the plume vector $\boldsymbol{a}_{\mathscr{P}}$ (4.1); the other two lines match the points (x_2^*, y_2^*) and (x_1^*, y_1^*) with the most distant point $(x, y) \in \mathscr{P}$.

which varies between 0 and 1 (see figure 7 for a sketch of a sheet-like thermal plume and its geometrical characteristics).

The plume vector

$$\boldsymbol{a}_{\mathscr{P}} = (x_1^* - x_2^*, y_1^* - y_2^*) \tag{4.1}$$

matches the most distant points in the plume $(x_1^*, y_1^*) \in \mathscr{P}$ and $(x_2^*, y_2^*) \in \mathscr{P}$, the coordinates of which satisfy the following equality

$$((x_1^* - x_2^*)^2 + (y_1^* - y_2^*)^2)^{1/2} = D_{\mathscr{P}}.$$

The vector product $\boldsymbol{e}_y \times \boldsymbol{a}_{\mathscr{P}}$ of the unit ordinate vector $\boldsymbol{e}_y$ (vertical direction in figure 6) and the plume vector $\boldsymbol{a}_{\mathscr{P}}$ points upward. Thus, the angle $\varphi_{\mathscr{P}}$ between the plume vector $\boldsymbol{a}_{\mathscr{P}}$ and the unit ordinate vector $\boldsymbol{e}_y$ varies in the interval $[0, \pi]$. The plume direction and its diameter are determined, respectively, by the direction and the length of the vector $\boldsymbol{a}_{\mathscr{P}}$.

To determine the curvature of the plume $\mathscr{P}$ we consider each non-degenerate triangle with the vertices $(x, y) \in \mathscr{P}$, (x_1^*, y_1^*) and (x_2^*, y_2^*) and the side lengths $D_{\mathscr{P}}$ and

$$D_{\mathscr{P},\beta} = \left((x_\beta^* - x)^2 + (y_\beta^* - y)^2\right)^{1/2} \quad (\beta = 1, 2).$$

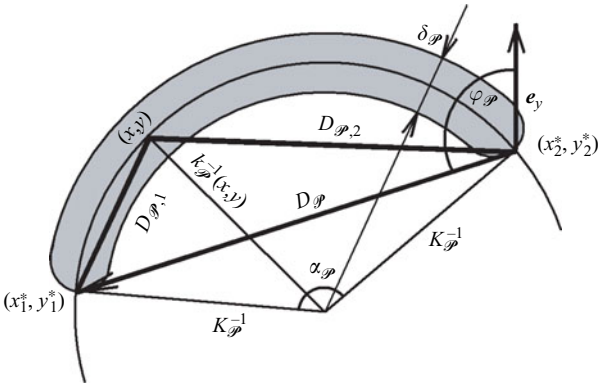

FIGURE 7. Sketch of a sheet-like thermal plume $\mathscr{P}$ (given in grey) with the thickness $\delta_{\mathscr{P}}$, diameter $D_{\mathscr{P}}$, curvature $K_{\mathscr{P}}$ and plume angle $\varphi_{\mathscr{P}}$.

The plume curvature $K_{\mathscr{P}}$,

$$K_{\mathscr{P}} = |\mathscr{P}|^{-1} \int_{\mathscr{P}} k_{\mathscr{P}}(x, y)\, \mathrm{d}\mathscr{P},$$

is defined then as the quantity $k_{\mathscr{P}}(x, y)$ averaged over the sheet-like plume $\mathscr{P}$, where the value of $k_{\mathscr{P}}(x, y)$ is inversely proportional to the circumradius of the considered triangle,

$$|k_{\mathscr{P}}(x, y)| = D_{\mathscr{P}}^{-1} D_{\mathscr{P},1}^{-1} D_{\mathscr{P},2}^{-1} ((D_{\mathscr{P}} + D_{\mathscr{P},1} + D_{\mathscr{P},2})(-D_{\mathscr{P}} + D_{\mathscr{P},1} + D_{\mathscr{P},2}) \times (D_{\mathscr{P}} - D_{\mathscr{P},1} + D_{\mathscr{P},2})(D_{\mathscr{P}} + D_{\mathscr{P},1} - D_{\mathscr{P},2}))^{1/2}.$$

The quantity $k_{\mathscr{P}}(x, y)$ is positive only if the point (x, y) is situated on the right-hand side of the plume vector $\boldsymbol{a}_{\mathscr{P}}$, i.e.

$$(x_1^* - x_2^*)(y - y_2^*) < (x - x_2^*)(y_1^* - y_2^*),$$

and non-positive otherwise. Generally, the absolute value of the plume curvature $K_{\mathscr{P}}$ does not exceed $2D_{\mathscr{P}}^{-1}$. The curvature of a straight-line plume is equal to zero, while that of a plume with the shape replicating the boundary of the horizontal cross-section S_z is equal to ± 2.

Further, we consider the isosceles triangle with the vertices (x_1^*, y_1^*), (x_2^*, y_2^*) and the circumcentre of the considered plume. The apical angle $\alpha_{\mathscr{P}}$ of this triangle equals

$$\alpha_{\mathscr{P}} = \arccos\left(1 - \frac{(K_{\mathscr{P}} D_{\mathscr{P}})^2}{2}\right).$$

Using the apical angle $\alpha_{\mathscr{P}}$, we can estimate the plume length $l_{\mathscr{P}}$ and the plume thickness $\delta_{\mathscr{P}}$ as follows

$$l_{\mathscr{P}} = \alpha_{\mathscr{P}} |K_{\mathscr{P}}|^{-1},$$
$$\delta_{\mathscr{P}} = \alpha_{\mathscr{P}}^{-1} |K_{\mathscr{P}}||\mathscr{P}|.$$

The plume aspect ratio, i.e. the ratio between the plume length and its thickness, is

$$\Gamma_{\mathscr{P}} = \frac{l_{\mathscr{P}}}{\delta_{\mathscr{P}}} = \frac{|\mathscr{P}|}{\delta_{\mathscr{P}}^2} = \alpha_{\mathscr{P}}^2 |K_{\mathscr{P}}|^{-2} |\mathscr{P}|^{-1}.$$

In table 1 the following geometrical characteristics of the sheet-like plumes depicted in figure 6 are presented: the plume area $A_{\mathscr{P}}$, diameter $D_{\mathscr{P}}$, curvature $K_{\mathscr{P}}$, thickness $\delta_{\mathscr{P}}$,

$\mathscr{N}_{\mathscr{P}}$	$A_{\mathscr{P}}$ $\times 10^{-3}$	$D_{\mathscr{P}}$ $\times 10^{-2}$	$K_{\mathscr{P}}$	$\delta_{\mathscr{P}}$ $\times 10^{-2}$	$\Gamma_{\mathscr{P}}$	$\varphi_{\mathscr{P}}$	$T_{\mathscr{P}}$ $\times 10^{-2}$	$\theta_{\mathscr{P}}$ $\times 10^{2}$	$\varepsilon_{\theta,\mathscr{P}}$ $\times 10^{-3}$	$u_{v,\mathscr{P}}$ $\times 10^{-2}$	$u_{h,\mathscr{P}}$ $\times 10^{-2}$	$\omega_{v,\mathscr{P}}$	$\omega_{h,\mathscr{P}}$
1	1.26	8.7	10.2	1.40	6.4	139	−18.2	7.18	2.00	−3.62	2.46	1.38	2.06
2	1.40	14.6	−2.0	0.96	15.3	106	−17.9	7.54	2.20	−3.82	2.32	0.68	1.98
3	1.15	13.1	−11.7	0.77	19.4	72	−17.9	7.21	2.15	−3.62	2.50	0.45	1.98
4	5.07	31.7	−0.6	1.60	19.8	78	−18.9	7.49	2.47	−3.61	2.21	0.50	2.05
5	1.15	8.7	8.5	1.30	6.8	78	−19.0	7.12	1.97	−3.35	2.98	0.95	2.72
6	1.38	16.5	−1.3	0.83	19.8	10	−18.8	7.51	2.20	−3.63	4.82	1.43	2.52
7	14.10	64.1	1.6	2.09	32.3	26	−19.5	7.43	2.29	−3.42	2.42	0.88	2.25
8	1.27	11.3	−4.9	1.11	10.3	35	−20.0	10.90	2.03	−4.87	6.44	2.95	3.12
9	1.13	14.3	4.4	0.77	18.9	29	−17.7	7.01	1.81	−3.65	6.87	1.16	2.90
10	0.95	9.5	15.1	0.90	11.8	104	−18.6	8.21	1.97	−3.96	2.02	0.63	2.10
11	1.34	14.9	−6.2	0.87	17.8	25	−17.6	7.17	1.87	−3.64	4.18	0.58	2.02
12	1.06	10.3	−5.7	1.02	10.2	91	−18.3	6.64	1.98	−3.27	4.54	0.42	2.47
13	2.98	19.3	7.3	1.39	15.4	143	−17.9	6.33	1.60	−3.18	2.40	0.64	2.08
14	5.22	21.7	−2.8	2.36	9.4	19	−20.2	8.03	2.46	−3.55	3.20	0.65	2.28
15	5.89	31.0	−0.5	1.90	16.4	150	−19.1	6.63	2.28	−3.18	0.92	0.83	1.93
16	9.79	50.3	0.4	1.94	25.9	167	−19.6	8.26	2.90	−3.84	1.72	0.56	2.23
17	2.25	11.6	−0.1	1.94	6.0	52	−20.5	8.66	2.40	−3.81	3.09	0.61	2.37
18	1.62	8.3	2.5	1.95	4.2	87	−19.5	10.67	1.84	−4.75	4.39	2.94	2.43
19	1.28	17.0	1.3	0.75	22.6	166	−19.8	5.87	3.03	−2.87	1.11	0.47	1.49
20	2.00	22.6	−3.2	0.87	26.6	111	−18.7	6.68	1.72	−3.30	2.62	0.54	2.77
21	1.11	13.7	12.0	0.69	23.0	140	−17.2	6.48	1.97	−3.46	4.13	0.41	2.09
22	0.90	16.4	4.4	0.54	31.1	71	−16.7	8.03	2.19	−4.46	4.63	0.81	1.86
23	6.94	36.9	−1.0	1.87	19.9	65	−19.3	7.14	2.59	−3.37	0.40	0.42	2.19
24	0.95	9.8	−0.9	0.97	10.1	147	−21.6	6.50	4.12	−2.74	2.88	1.10	2.03
25	1.03	19.2	1.8	0.53	36.4	39	−17.9	3.41	3.31	−1.76	0.46	0.73	1.65
26	1.13	10.9	9.7	0.98	11.6	61	−18.4	6.48	2.59	−3.28	3.21	0.49	2.11
27	1.04	11.7	−14.5	0.74	18.7	170	−17.6	7.30	1.89	−3.73	3.04	0.42	1.99
28	1.24	7.1	−1.9	1.75	4.0	172	−20.6	9.09	2.54	−3.82	1.59	0.43	2.02

TABLE 1. Plume characteristics due to their numeration $\mathscr{N}_{\mathscr{P}}$ for the case $Ra = 2 \times 10^9$, $Pr = 5.4$, $\Gamma = 1$, $T_{thr}^{-} = -0.14$ at distance $z = H/Nu$ from the top plate (see figure 6). $A_{\mathscr{P}}$ denotes the area, $D_{\mathscr{P}}$ diameter, $K_{\mathscr{P}}$ curvature, $\delta_{\mathscr{P}}$ thickness, $\Gamma_{\mathscr{P}}$ aspect ratio, $T_{\mathscr{P}}$ temperature, $\theta_{\mathscr{P}}$ heat flux, $\varepsilon_{\theta,\mathscr{P}}$ thermal dissipation rate, $u_{v,\mathscr{P}}$ vertical velocity, $u_{h,\mathscr{P}}$ absolute value of the horizontal velocity, $\omega_{v,\mathscr{P}}$ absolute value of the vertical vorticity and $\omega_{h,\mathscr{P}}$ absolute value of the horizontal vorticity and $\varphi_{\mathscr{P}}$ is the angle (in degrees) between the plume $\mathscr{P}$ and the ordinate axis.

aspect ratio $\Gamma_{\mathscr{P}}$ and the angle $\varphi_{\mathscr{P}}$ between the plume and the ordinate axis. Comparing different plumes in table 1 and figure 6 it is found that the plumes with large area usually have a large diameter (for example, the plume number 7). The smallest plume diameter (plume number 28) is 14 times smaller than the diameter of the considered cross-section. The plume curvature is negative (plumes 3, 20, 27) or positive (plumes 9, 10, 22) if the plume is located mostly to the left or to the right of the plume vector (see also figure 6). If the plume vector divides the plume into two relatively equal parts, the plume curvature is close to zero (as for the plume number 17). The absolute value of the plume curvature can be more than 7 times larger than the curvature of the Rayleigh–Bénard cell (plumes 10 and 27). The plumes, which are located in the vicinity of the cell boundary and almost replicate its form, have the absolute value of the plume curvature close to 2 (as plume 25). Elongated plumes are usually rather thin (as plumes 22 and 25) with a plume thickness which is up to 200 times smaller than the diameter of the cell. For the plumes with a complicated form (as plume 14),

the plume thickness can be relatively large. The plume aspect ratio can exceed 30 (as for plumes 7 and 25). The angle between the plume and the ordinate axis varies within the interval $[0, \pi]$ and no preferable value is observed.

In figure 8, the probability density functions of the logarithms of the plume area, diameter, curvature, thickness and aspect ratio evaluated for $Ra = 2 \times 10^9$ and 2×10^{10}, $Pr = 5.4$, $\Gamma = 1$ and distances $z = 0.5H/Nu$, $z = H/Nu$, $z = 0.5H$, $z = H - H/Nu$ and $z = H - 0.5H/Nu$ from the top plate are presented. From the graphs of these quantities, we can estimate the ranges of their possible values. Approximately 4.0×10^5 and 9.3×10^5 sheet-like thermal plumes were investigated in the cases $Ra = 2 \times 10^9$ and 2×10^{10}, respectively. In all graphs in figure 8 the bin widths equal 1/20 of the considered intervals. The p.d.f. graphs of the plume area are 'cut off' from the left (figure 8*a*, *d*), since the plumes that we consider have an area larger than 2×10^{-4}.

Although the probability density functions of the plume area or plume aspect ratio look like log-normal distributions, the graphics for the other obtained quantities are non-symmetric (see, for example, p.d.f. of the plume curvature on figure 8*c*, *f*). With increasing distance from the horizontal plates in the regions $z \in [0, H/Nu]$ and $z \in [H - H/Nu, H]$ the ranges of the possible values for the plume area (figure 8*d*), diameter (figure 8*e*), thickness (figure 8*j*) and aspect ratio (figure 8*k*) decrease, while that for the curvature (figure 8*f*) increases.

The mean thickness of the sheet-like thermal plumes is equal to the thickness of the thermal boundary layers in both cases considered, i.e. it is of order $0.5H/Nu$.

5. Physical properties of the sheet-like plumes

The sheet-like plumes are generally characterized by high absolute values of the temperature, vertical velocity component, local heat flux and vertical vorticity component as was concluded from the analysis of conditionally averaged plume characteristics in § 3. In this section, we investigate the sheet-like plumes in more detail based on our DNS and LES data.

In figure 9, snapshots of the heat flux θ, thermal dissipation rate ε_θ and the vorticity norm

$$\omega = \left(\omega_x^2 + \omega_y^2 + \omega_z^2\right)^{1/2}$$

are presented for the case $Ra = 2 \times 10^9$, $Pr = 5.4$, $\Gamma = 1$ in the horizontal cross-section at distance $z = H/Nu$ from the top plate. Here z is the vertical and x and y the horizontal directions. These snapshots correspond to the instantaneous temperature distribution presented in figure 3(*a*). Since the sheet-like thermal plumes are indicated also by large values of the conditionally averaged heat flux (see figure 5*c*), the regions of high absolute values of the temperature in figure 3(*a*) almost coincide with the regions with large local heat flux in figure 9(*a*). The borders of the sheet-like thermal plumes are reflected by high values of the thermal dissipation rate in figure 9(*b*). Large values of the vorticity norm (see figure 9*c*) are also obtained close to the borders of the sheet-like plumes owing to high absolute ω_h values or even on the whole plume body owing to relatively large absolute ω_v values.

In figure 10, a snapshot of the vertical vorticity component ω_v is presented for the same case as in figure 9 together with superimposed velocity vectors. While moving along the elongated sheet-like plume, we find negative values of the vertical vorticity (shown in blue) on the right-hand side of the plume and positive values on the left-hand side (shown in red). This is because the cold sheet-like plume, i.e. the part

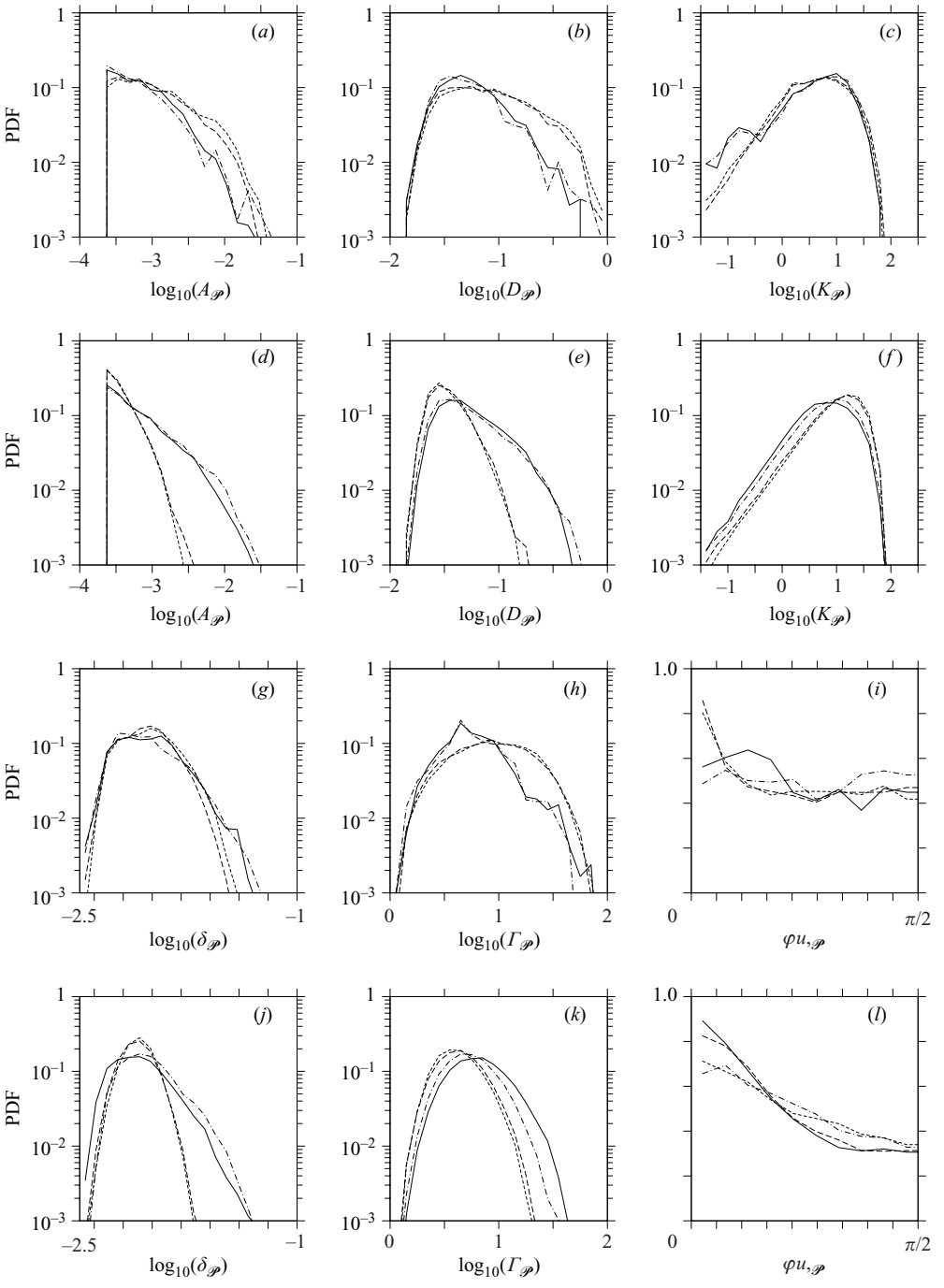

FIGURE 8. Probability density functions of the logarithms of the following geometrical characteristics of the sheet-like thermal plumes: (a, d) area, (b, e) diameter, (c, f) curvature, (g, j) thickness, (h, k) aspect ratio and (i, l) probability density function of the angle between the plume direction and the horizontal component of its velocity vector, evaluated for $Ra = 2 \times 10^9$ $(a–c, g–i)$ and $Ra = 2 \times 10^{10}$ $(d–f, j–l)$, $Pr = 5.4$, $\Gamma = 1$ and distances $z = 0.5H/Nu$ (——), $z = H/Nu$ (– – –), $z = H - H/Nu$ (- - -) and $z = H - 0.5H/Nu$ (– · –) from the top plate.

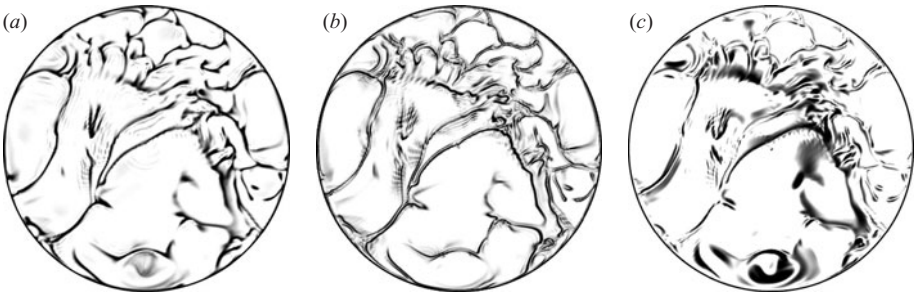

FIGURE 9. Snapshots of (a) the heat flux θ, (b) thermal dissipation rate ε_θ and (c) the vorticity norm ω for $Ra = 2 \times 10^9$, $Pr = 5.4$, $\Gamma = 1$ in the horizontal cross-section at distance $z = H/Nu$ from the top plate. The colour scale rages from white (zero) to black (positive values larger than (a) $3Nu$, (b) $0.1\varepsilon_{\theta,max}$ and (c) $0.3\omega_{max}$).

of the fluid restricted by the 'red' and 'blue' borders of the sheet-like plume, moves towards the bottom of the Rayleigh–Bénard cell.

In figure 11, some of the plumes from figure 6 are presented together with the vorticity vectors. We can see that on one border of any elongated sheet-like plume the vorticity vector points along the plume, while on the opposite side of the plume the vorticity vector points in the opposite direction. This shows that large absolute values of the horizontal vorticity component usually indicate the borders of the sheet-like plumes, as was shown in the analysis of the conditionally averaged horizontal vorticity component in § 3.

Some of the sheet-like plumes collide with other plumes while moving in horizontal directions. In this case, they merge and swirl to form the stems of the mushroom-like plumes which develop in the bulk of the Rayleigh–Bénard cell. The regions of their convolution are characterized by high absolute values of the vertical vorticity component (see, for example, figure 11f).

In table 1, the following physical characteristics of the plumes given in figure 6 are presented: the plume temperature $T_{\mathscr{P}}$, local heat flux $\theta_{\mathscr{P}}$ and thermal dissipation rate $\varepsilon_{\theta,\mathscr{P}}$,

$$T_{\mathscr{P}} = |\mathscr{P}|^{-1} \int_{\mathscr{P}} T(x, y)\, \mathrm{d}\mathscr{P}, \quad \theta_{\mathscr{P}} = |\mathscr{P}|^{-1} \int_{\mathscr{P}} \theta(x, y)\, \mathrm{d}\mathscr{P}, \quad \varepsilon_{\theta,\mathscr{P}} = |\mathscr{P}|^{-1} \int_{\mathscr{P}} \varepsilon_\theta(x, y)\, \mathrm{d}\mathscr{P},$$

the plume vertical velocity component $u_{v,\mathscr{P}}$ and absolute value of the horizontal velocity component $u_{h,\mathscr{P}}$,

$$u_{v,\mathscr{P}} = |\mathscr{P}|^{-1} \int_{\mathscr{P}} u_z(x, y)\, \mathrm{d}\mathscr{P}, \quad u_{h,\mathscr{P}} = |\mathscr{P}|^{-1} \int_{\mathscr{P}} \left(u_x^2(x, y) + u_y^2(x, y)\right)^{1/2} \mathrm{d}\mathscr{P},$$

together with the absolute values of the vertical $\omega_{v,\mathscr{P}}$ and horizontal $\omega_{h,\mathscr{P}}$ vorticity components, calculated as follows

$$\omega_{v,\mathscr{P}} = |\mathscr{P}|^{-1} \int_{\mathscr{P}} |\omega_z(x, y)|\, \mathrm{d}\mathscr{P}, \quad \omega_{h,\mathscr{P}} = |\mathscr{P}|^{-1} \int_{\mathscr{P}} \left(\omega_x^2(x, y) + \omega_y^2(x, y)\right)^{1/2} \mathrm{d}\mathscr{P}.$$

From table 1, it can be concluded that the largest values of the plume heat flux are obtained for the plumes with highest absolute values of the vertical components of the velocity and vorticity. These are the swirling plumes 8 and 18 which serve in the bulk as the stems of the mushroom-like plumes.

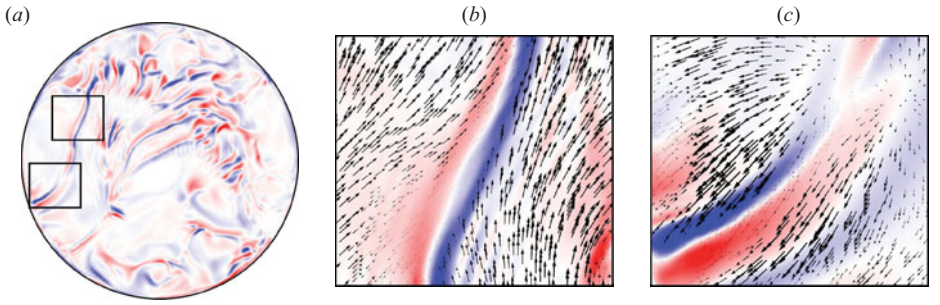

FIGURE 10. A snapshot of the vertical vorticity ω_v for $Ra = 2 \times 10^9$, $Pr = 5.4$, $\Gamma = 1$ (a) in horizontal cross-section at distance $z = H/Nu$ from the top plate and (b, c) its close-up views with superimposed velocity vectors. The colour scale ranges from blue (negative values) through white (zero) to red (positive values).

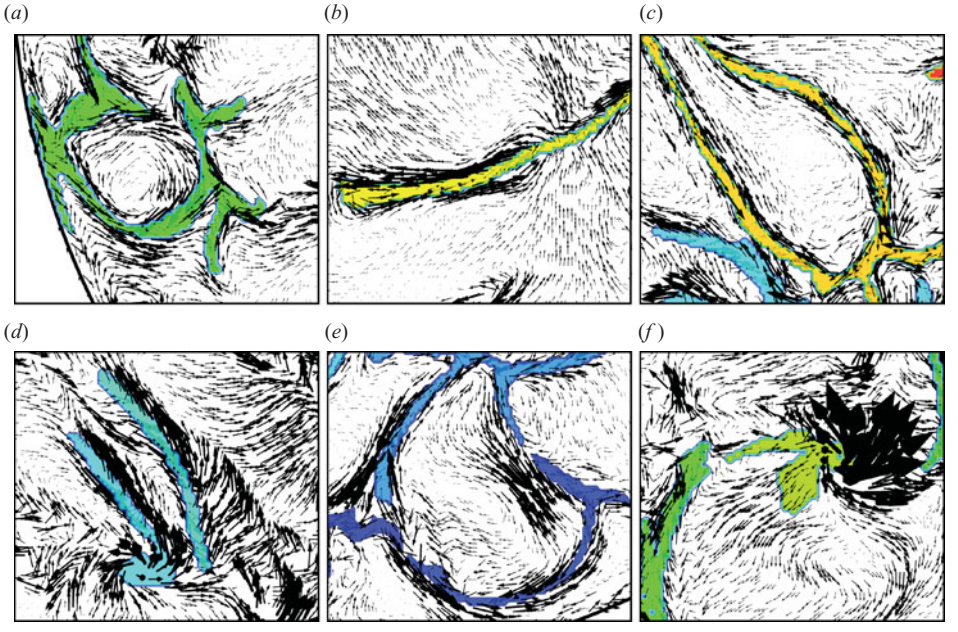

FIGURE 11. Close-up views of the sheet-like thermal plumes numbered (a) 14, (b) 20, (c) 23, (d) 8 and 9, (e) 2 and 4, (f) 15 and 18 from figure 6 with superimposed vorticity vectors. The colour scale is as figure 6.

In figure 8(i, l) the probability density functions of the angle between the plume vector and the plume velocity in the horizontal direction are presented. We can see that at the distances $z = N/Nu$ and $z = H - H/Nu$ from the top plate, this angle is close to zero for most of the cases. Thus, in this horizontal cross-section the fluid inside the sheet-like plumes moves predominantly along the plumes.

We supplement our investigation of the sheet-like plumes by evaluation of the probability density functions of the sheet-like plume temperature, heat flux, logarithm of the thermal dissipation rate (figure 12), horizontal and vertical velocity components (figure 13a–f) and logarithms of the absolute values of the horizontal and vertical vorticity components (figure 13g–l), obtained for $Ra = 2 \times 10^9$ and 2×10^{10}, $Pr = 5.4$,

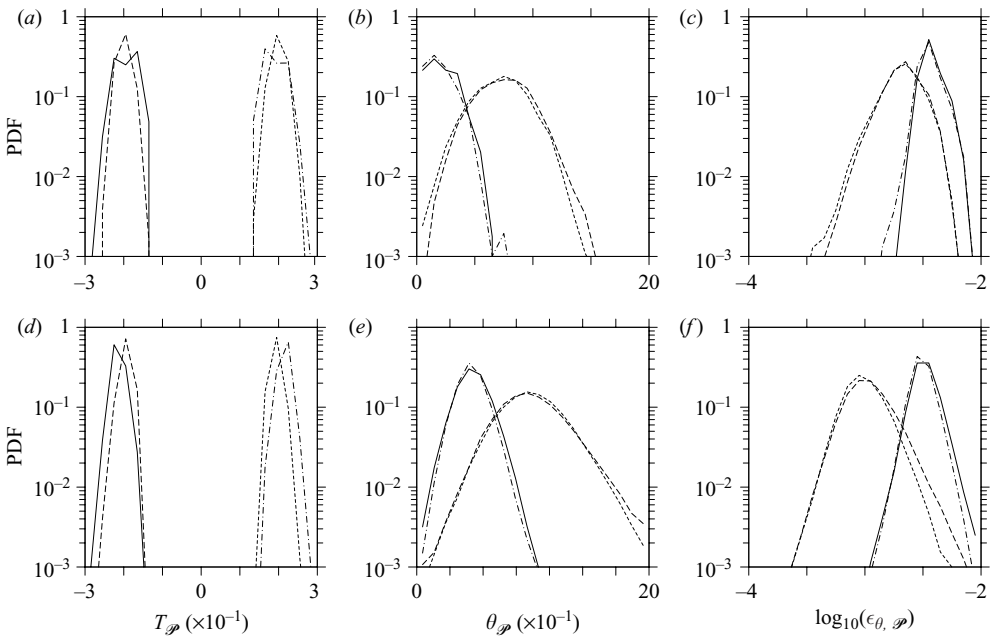

FIGURE 12. Probability density functions of the following characteristics of the sheet-like thermal plumes: (a, d) temperature, (b, e) heat flux and (c, f) logarithm of the thermal dissipation rate, evaluated for $Ra = 2 \times 10^9$ $(a–c)$ and $Ra = 2 \times 10^{10}$ $(d–f)$, $Pr = 5.4$, $\Gamma = 1$ and distances $z = 0.5H/Nu$ (——), $z = H/Nu$ (– – –), $z = H - H/Nu$ (- - -) and $z = H - 0.5H/Nu$ (– · –) from the top plate.

$\Gamma = 1$ at different distances from the top plate. Comparing the p.d.f. of the plume local heat flux for different distances from the top plate and different Rayleigh numbers (figure 12b, e) we conclude that the range of possible values of the plume local heat flux increases with increasing Rayleigh number and while moving away from the plates towards the bulk. The values of the plume thermal dissipation rate (figure 12c, f) generally decrease with increasing distance from the considered cross-section to the nearest horizontal boundary of the domain.

In order to estimate quantitatively the contribution of the sheet-like thermal plumes to the mean heat transport, we consider the functions $\langle \theta\ \vartheta \rangle_{t,S_z}$ and $\langle \epsilon_\theta\ \vartheta \rangle_{t,S_z}$ presented in figure 14 for the case $Ra = 2 \times 10^9$ and different distances from the top plate. These graphs illustrate which temperatures contribute more to the mean heat flux and to the mean thermal dissipation rate, both averaged in time and over considered horizontal cross-sections. For a fixed horizontal cross-section S_z, the functions $\langle \theta\ \vartheta \rangle_{t,S_z}$ and $\langle \epsilon_\theta\ \vartheta \rangle_{t,S_z}$, averaged for all temperatures $T \in [-0.5; 0.5]$, give the mean heat flux (the Nusselt number) and the mean thermal dissipation rate, respectively. In contrast to the mean heat flux, the mean thermal dissipation rate depends strongly on the distance from the nearest horizontal plate and the following relation holds $\langle \epsilon_\theta \rangle_{t,z=0} > \langle \epsilon_\theta \rangle_{t,z=H/2} Nu$, as was proved analytically in Shishkina & Wagner (2006).

To calculate the contribution of the sheet-like thermal plumes to the mean heat flux and the mean thermal dissipation rate close to the top plate, we should average, respectively, $\langle \theta\ \vartheta \rangle_{t,S_z}$ and $\langle \epsilon_\theta\ \vartheta \rangle_{t,S_z}$ over the temperature interval $[-0.5; T^-_{thr}]$, where T^-_{thr} is the temperature threshold used to extract the sheet-like plumes. Although the sheet-like thermal plumes account for the dominating part of the mean heat flux, the largest part of the the mean thermal dissipation rate corresponds to the turbulent

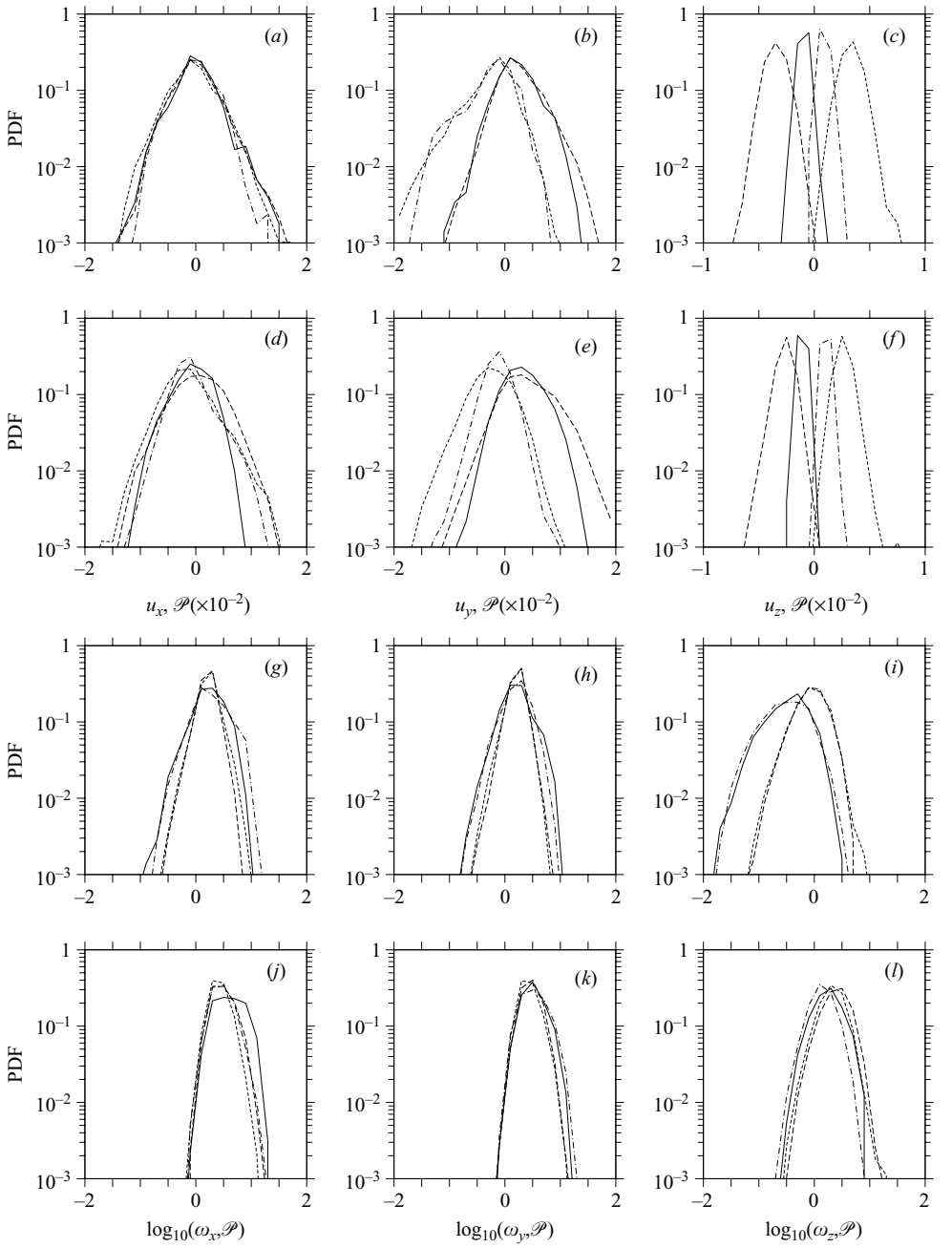

FIGURE 13. Probability density functions of the following characteristics of the sheet-like thermal plumes: (a, b, d, e) horizontal and (c, f) vertical components of the velocity; logarithms of the absolute values of the (g, h, j, k) horizontal and (i, l) vertical components of the vorticity, evaluated for $Ra = 2 \times 10^9$ $(a–c, g–i)$ and $Ra = 2 \times 10^{10}$ $(d–f, j–l)$, $Pr = 5.4$, $\Gamma = 1$ and distances $z = 0.5H/Nu$ (——), $z = H/Nu$ (– – –), $z = H - H/Nu$ (- - -) and $z = H - 0.5H/Nu$ (– · –) from the top plate.

background. In particular, in the case $Ra = 2 \times 10^9$ the sheet-like thermal plumes cover less than 21% of the horizontal cross-section at the border between the upper thermal boundary layer and the bulk, while they account for about 84% of the

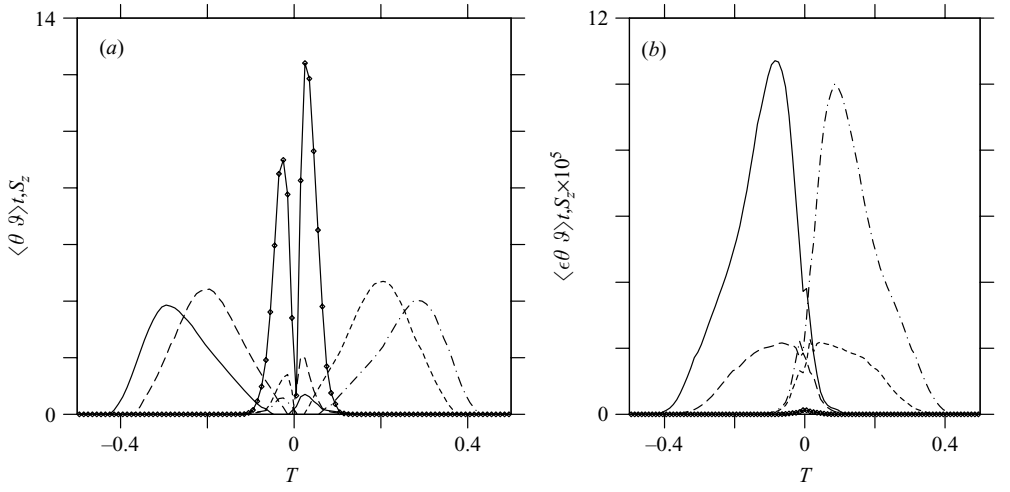

FIGURE 14. Temperature contributions to (*a*) the mean heat flux and to (*b*) the mean thermal dissipation rate, evaluated for $Ra = 2 \times 10^9$, $Pr = 5.4$, $\Gamma = 1$ and distances $z = 0.5H/Nu$ (——), $z = H/Nu$ (– – –), $z = H/2$ (—•—), $z = H(1 - 1/Nu)$ (- - -) $z = H(1 - 0.5/Nu)$ (– · –) from the top plate.

Ra	2×10^9	2×10^9	2×10^{10}	2×10^{10}
z	$\lvert S_z\rvert$	$\langle\theta\rangle_{t,S_z}$	$\lvert S_z\rvert$	$\langle\theta\rangle_{t,S_z}$
$0.5H/Nu$	20.9	83.9	20.8	67.3
H/Nu	11.3	75.6	12.5	63.0

TABLE 2. Portions (in %) of the area of a horizontal cross-section S_z, covered by the sheet-like thermal plumes and the mean contributions (in %) of the sheet-like thermal plumes to the mean heat flux θ averaged in time and over the horizontal cross-sections at the distances $z = 0.5H/Nu$ and $z = H/Nu$ from the top plate, evaluated for $Ra = 2 \times 10^9$ and 2×10^{10}, $Pr = 5.4$, $\Gamma = 1$.

mean heat flux and 29% of the mean thermal dissipation rate (see also table 2 for $Ra = 2 \times 10^9$ and 2×10^{10}).

6. Conclusions

Sheet-like thermal plumes which develop in turbulent Rayleigh–Bénard convection of water with Prandtl number $Pr = 5.4$ in a cylindrical container with the aspect ratio $\Gamma = 1$ were studied using the data of the direct numerical simulations for the Rayleigh number $Ra = 2 \times 10^9$ and well-resolved large-eddy simulations for the case $Ra = 2 \times 10^{10}$.

The choice of the temperature threshold to extract the sheet-like plumes was based on the analysis of the dependences on the temperature of the local heat flux, thermal dissipation rate and spatial components of the velocity and vorticity fields in different horizontal cross-sections. These time-averaged dependencies on the temperature were called the conditionally averaged quantities. It was shown that the optimum temperature threshold to extract the sheet-like thermal plumes at the borders between the thermal boundary layers and the bulk is the point of the

maximum of the conditionally averaged thermal dissipation rate. Since high values of the conditionally averaged absolute values of the horizontal vorticity component also indicate the borders of the sheet-like thermal plumes, the maximum value of the conditionally averaged absolute value of the horizontal vorticity component can be used as the temperature threshold to extract the thermal plumes in the bulk.

The formulae to compute the sheet-like plume curvature, thickness, length and aspect ratio were introduced. Based on the DNS and LES data and the above formulae, the probability density functions of the geometrical properties of the sheet-like thermal plumes such as plume area, diameter, curvature, thickness, length and aspect ratio together with the probability density functions of physical properties of the plumes like temperature, heat flux, thermal dissipation rate, velocity and vorticity were investigated. In particular, it was shown that with growing distance from the nearest horizontal plate the sheet-like thermal plume area, diameter and thermal dissipation rate generally decrease, while the sheet-like thermal plume curvature and local vertical heat flux increase. The mean thickness of the sheet-like thermal plumes is approximately equal to the thickness of the thermal boundary layers, i.e. $0.5H/Nu$.

It was shown that the sheet-like plumes are characterized by relatively large absolute values of the vertical velocity component, local heat flux and vertical vorticity component. The borders of these plumes are indicated by large values of the thermal dissipation rate and the norm of the vorticity. Predominantly horizontal directions of the vorticity vectors which point along the elongated sheet-like thermal plumes also characterize the borders of these plumes.

The sheet-like thermal plumes play an important role in heat transport. They correspond to a relatively small part of the area ($\approx$21%) of the horizontal cross-section at a distance $z = 0.5H/Nu$ from the top or bottom plates, which separate the thermal boundary layers and the bulk, while accounting for the dominating part of the mean heat flux ($\approx$84% in the case for $Ra = 2 \times 10^9$).

Extremely high values of the local heat flux and high absolute values of the vertical velocity and the vertical vorticity components are obtained in the regions where the sheet-like plumes merge and convolute. Fluid swirling at these places forms the stems of the mushroom-like thermal plumes which develop in the bulk of the Rayleigh–Bénard cell.

The authors are grateful to Professor K.-Q. Xia and Professor A. Thess for helpful discussions.

REFERENCES

Ahlers, G. 2005 Experiments with Rayleigh–Bénard convection. In *Dynamics of Spatiotemporal Structures – Henri Benard Centenary Review* (ed. I. Mutabazi, E. Guyon & J. E. Wesfreid). Springer.

Ahlers, G., Brown, E., Araujo, F. F., Funfschilling, D., Grossmann, S. & Lohse, D. 2006 Non-Oberbeck–Boussinesq effects in strongly turbulent Rayleigh–Bénard convection. *J. Fluid Mech.* **569**, 409–445.

Belmonte, A. & Libchaber, A. 1996 Thermal signature of plumes in turbulent convection: the skewness of the derivative. *Phys. Rev.* E **53**, 4893–4898.

Ching, E. S. C., Guo, H., Shang, X.-D., Tong, P. & Xia, K.-Q. 2004 Extraction of plumes in turbulent thermal convection. *Phys. Rev. Lett.* **93**, 124501.

Cortese, T. & Balachandar, S. 1993 Vortical nature of thermal plumes in turbulent convection. *Phys. Fluids* **5** (12), 3226–3232.

Funfschilling, D. & Ahlers, G. 2004 Plume motion and large-scale circulation in a cylindrical Rayleigh–Bénard cell. *Phys. Rev. Lett.* **92**, 194502.

Funfschilling, D., Brown, E., Nikolaenko, A. & Ahlers, G. 2005 Heat transport by turbulent Rayleigh–Bénard convection in cylindrical samples with aspect ratio one and larger. *J. Fluid Mech.* **536**, 145–154.

Gray, D. D. & Giorgini, A. 1976 The validity of the Boussinesq approximation for liquids and gases. *Intl J. Heat Mass Transer* **19**, 545–551.

Grossmann, S. & Lohse, D. 2000 Scaling in thermal convection: a unifying theory. *J. Fluid Mech.* **407**, 27–56.

Grossmann, S. & Lohse, D. 2004 Fluctuations in turbulent Rayleigh–Bénard convection: the role of plumes. *Phys. Fluids* **16**, 4462–4472.

Grötzbach, G. 1983 Spatial resolution requirements for direct numerical simulation of Rayleigh–Bénard convection. *J. Comput. Phys.* **49**, 241–264.

Haramina, T. & Tilgner, A. 2004 Coherent structures in boundary layers of Rayleigh–Bénard convection. *Phys. Rev.* E **69**, 056306.

Hartlep, T., Tilgner, A. & Busse, F. H. 2005 Transition to turbulent convection in a fluid layer heated from below at moderate aspect ratio. *J. Fluid Mech.* **544**, 309–322.

Juliem, K., Legg, S., McWilliams, J. & Werne, J. 1999 Plumes in rotating convection. Part 1. Ensemble statistics and dynamical balances. *J. Fluid Mech.* **391**, 151–187.

Kadanoff, L. P. 2001 Turbulent heat flow: structures and scaling. *Phys. Today* **54**, 34–39.

Leonard, A. & Winckelmans, G. S. 1999 A tensor-diffusivity subgrid model for large-eddy simulation. *Caltech ASCI Tech. Rep.* 043.

Lui, S.-L. & Xia K.-Q. 1998 Spatial structure of the thermal boundary layer in turbulent convection. *Phys. Rev.* E **57**, 5494–5503.

du Puits, R., Resagk, C., Tilgner, A., Busse, F. H. & Thess, A. 2007 Structure of thermal boundary layers in turbulent Rayleigh–Bénard convection. *J. Fluid Mech.* **572**, 231–254.

Puthenveettil, B. A. & Arakeri, J. H. 2005 Plume structure in high-Rayleigh-number convection. *J. Fluid Mech.* **542**, 217–249.

Shang, X.-D., Qiu, X.-L., Tong, P. & Xia, K.-Q. 2004 Measurements of the local convective heat flux in turbulent Rayleigh–Bénard convection. *Phys. Rev.* E **70**, 026308.

Shishkina, O. & Wagner, C. 2006 Analysis of thermal dissipation rates in turbulent Rayleigh–Bénard convection. *J. Fluid Mech.*, **546**, 51–60.

Shishkina, O. & Wagner, C. 2007*a* A fourth order finite volume scheme for turbulent flow simulations in cylindrical domains. *Computers Fluids* **36**, 484–497.

Shishkina, O. & Wagner, C. 2007*b* Local heat fluxes in turbulent Rayleigh–Bénard convection. *Phys. Fluids* **19**, 085107.

Shishkina, O. & Wagner, C. 2007*c* Boundary and interior layers in turbulent thermal convection in cylindrical containers. *Intl J. Comput. Sci. Maths* **1**, 360–373.

Siggia, E. D. 1994 High Rayleigh number convection. *Annu. Rev. Fluid Mech.* **26**, 137–168.

Sparrow, E. M., Husar, R. B. & Goldstein, R. J. 1970 Observations and other characteristics of thermals. *J. Fluid Mech.* **41**, 793–800.

Verzicco, R. & Camussi, R. 2003 Numerical experiments on strongly turbulent thermal convection in a slender cylindrical cell. *J. Fluid Mech.* **477**, 19–49.

Xi, H.-D., Lam, S. & Xia, K.-Q. 2004 From laminar plumes to organized flows: the onset of large-scale circulation in turbulent thermal convection. *J. Fluid Mech.* **503**, 47–56.

Zahn, J.-P. 2000 Plumes in stellar convection zones. *Ann. NY Acad. Sci.* **898**, 90–104.

Zhou, S.-Q. & Xia K.-Q. 2002 Plume statistics in thermal turbulence: mixing of an active scalar. *Phys. Rev. Lett.* **89**, 184502.

Zhou, Q., Sun, C. & Xia, K.-Q. 2007 Morphological evolution of thermal plumes in turbulent Rayleigh–Bénard convection. *Phys. Rev. Lett.* **98**, 074501.

Zocchi, G., Moses, E. & Libchaber, A. 1990 Coherent structures in turbulent convection, an experimental study. *Physica* A **166**, 387–407.